Friction

Research Article

Toward lithium-free tribology: Design and performance of plant oil-based greases thickened with functionalized nanoclays

Mohammad Eskandari[1,2], Ali Zayaan Macknojia[1], Asghar Shirani[1], Kent Chapman[2,3], Diana Berman[1,2]✉

Cite this article: Eskandari M, Macknojia A Z, Shirani A, et al. *Friction* 2026, **14**(6): 9441204. https://doi.org/10.26599/FRICT.2025.9441204

ABSTRACT: To address the persistent environmental concerns of petroleum-based lubricants, we report on a new class of high-performance, sustainable greases. These were formulated by combining select vegetable oils, including the structurally unique *Orychophragmus violaceus* (OV) seed oil, with an oleic acid-functionalized organo-modified montmorillonite nanoclay thickener. The sustainable samples consistently outperformed an industrial-grade lithium soap grease in tribological experiments. Remarkably, under harsh conditions of high load (up to 500 N) and temperature (150 °C), both 5 and 10 wt% nanoclay-thickened OV-based greases exhibited superlubricity, with the coefficient of friction (COF) of approximately 0.008. Surface analysis using Raman spectroscopy after the tribological experiments revealed that this exceptional performance was not a result of typical carbon-based tribofilm formation but from a novel lubrication mechanism: the *in-situ* formation of an adhesive, low-shear solid tribofilm composed of the nanoclay itself. The formulated greases also exhibited excellent low-temperature fluidity and structural stability, with complete recovery after freeze-thaw cycles to −20 °C. These results highlight a new design methodology for creating reliable and biodegradable lubricants suitable for extreme industrial applications.

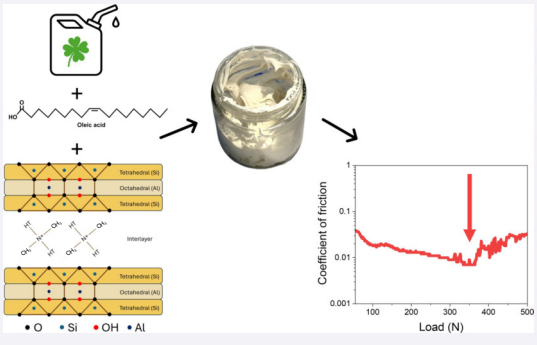

KEYWORDS: tribology; lubricating grease; organo-modified nanoclays; *Orychophragmus violaceus* (OV); vegetable oil; superlubricity

1 Introduction

Approximately 30% of the world's primary energy consumption is attributed to friction, leading to economic losses that can account for 2%–7% of a country's GDP annually [1]. Furthermore, friction and wear cause about 119 EJ (119×10^{18} J) of energy loss, with 103 EJ used to overcome friction and 16 EJ for re-manufacturing worn parts [2]. Addressing friction and wear issues using surface engineering [3, 4], material selection [5], and lubrication technologies using either liquid [6, 7], semi-solid [8, 9], or solid [10] lubricants might decrease these numbers by 40% over the long run (15 years) and by 18% in the short term (8 years) [11]. Among these, the most effective and widely used method for reducing friction and wear and extending the lifespan of modern mechanical systems is the introduction of a lubricant into sliding contacts [12].

Conventional lubricants, mainly petroleum-based, pose significant health and safety concerns across their lifecycle [2] as a result of potential cross-contamination and long-term pollution during production and use [12, 13]. When it comes to grease lubrication, which is critically important for use in heavy machinery, bearings, and high-pressure seals, biocompatibility problems are even more pronounced. Lubricating greases are complex formulations consisting of three main components: base oil, thickener, and additives [14, 15]. The base oil, which is typically mineral or synthetic, carries the primary tribological responsibility [16]. Thickeners, soap-based (e.g., lithium, calcium) or non-soap (e.g., clay, polytetrafluoroethylene (PTFE)), form a three-dimensional network that immobilizes the oil; greases are described to be similar to a sponge soaked with a liquid lubricant [14, 15]. Additives enhance specific properties and performance characteristics of greases, such as preventing corrosion and high-temperature oxidation, withstanding extreme pressures, and diminishing wear and friction [14, 17]. Grease formulation requires a careful selection of components to meet specific application requirements. Despite much progress in combining ecologically friendly materials with better lubricant performance, there has not been much progress, and today's grease market is

[1] Department of Materials Science and Engineering, University of North Texas, Denton, TX76205, USA. [2] BioDiscovery Institute, University of North Texas, Denton, TX76205, USA. [3] Department of Biological Sciences, University of North Texas, Denton, TX76205, USA.

✉ Corresponding author. E-mail: Diana.Berman@unt.edu

Received: August 13, 2025; Revised: December 3, 2025; Accepted: December 12, 2025

extensively governed by the use of non-renewable, non-biodegradable, toxic, bioaccumulative, and therefore environmentally unfriendly oils and soaps [18, 19].

Recent research has focused on replacing the three main components of greases. For base oils, synthetic esters and vegetable oils (biodegradability up to 100%) are being developed as alternatives to traditional oils (≤ 40% biodegradability) [18, 20]. Synthetic esters provide non-toxicity, biodegradability, hydrolytic stability, and consistent properties [20]. Vegetable oils combine excellent biodegradability with high viscosity index, lubricity, low volatility, and shear stability, while also being less reactive with metals [12]. Rapeseed oil, rich in oleic acid, is widely used in Europe for hydraulic devices and chainsaws [18], with similar uses for sunflower oil [21]. High-erucic rapeseed species [22, 23], castor oil and its 12-hydroxystearate soaps [12, 23], as well as oils from palm, coconut, crambe, meadowfoam, *Lesquerella*, and *pennycress* have also shown promise [24, 25]. However, biolubricants often suffer from poor aging resistance due to unsaturated fatty acids and ester groups, which oxidize at high temperatures [7, 12]. Even conventional greases face low oxidation resistance [26]. Hydrolytic degradation of crop oils can also yield acidic products that cause corrosion and alter base fluid properties [27].

Orychophragmus violaceus (OV) seed oil [24], recently reported as highly viscous, contains unusual long-chain dihydroxy fatty acids primarily in the form of triacylglycerol (TAG) estolides [28, 29]. These complex estolides give OV oil superior high-temperature tribological performance compared to castor oil, which contains far fewer estolides [24, 28]. Estolides offer higher oxidative stability, greater lubricity, and better low-temperature properties than conventional petroleum oils [30].

For grease thickeners, bio-friendly options under study include natural polymers (cellulose, lignin, and chitosan) [31, 32], biodegradable synthetic polymers (polyhydroxyalkanoates, polyurea, and sorbitan monostearate) [33–35], and biodegradable nanomaterials [36–38]. Polyurea remains the most important organic non-soap thickener, while organo-clays are the leading inorganic option [18]. Fine clays like bentonite, mainly montmorillonite, have been used since the early 20th century to improve high-temperature performance, though their lack of a fibrous structure reduces stability [23]. Montmorillonite, a layered silicate of aluminum oxide and silicon oxide, can be modified by exchanging hydrophilic cations (e.g., Na^+) with large organic cations (e.g., quaternary ammonium salts), increasing hydrophobicity [39, 40]. This well-established strategy enhances grease stability and broadens functionality across applications [41]. Cloisite, a modified montmorillonite, has therefore gained strong academic interest as a bio-friendly grease thickener [8, 40, 42].

This study reports the design and creation of greases from three plant-based (castor, rapeseed, and OV) oils thickened with oleic acid-functionalized nanoclay (Cloisite 20A). Two different thickener loadings were used with the respective oils. Comprehensive performance experiments were conducted to assess the tribological behavior of each sample from different perspectives. Comparisons with a model industrial-grade lithium soap grease revealed the exceptional performance of the designed lubricants, which even surpassed that of the base oil at some points.

2 Materials and methods

2.1 Starting materials

Three types of vegetable seed oils, namely high erucic acid rapeseed (HEAR), castor, and OV, along with PAO10 synthetic oil, were selected as the base oils for grease creation. PAO10 oil was used for comparison with the plant-based oils. HEAR oil was commercially available, castor oil was purchased from Sigma Aldrich, USA, and PAO10 was provided by Tulstar, USA. The steps in OV oil processing have been explained elsewhere [24, 28, 43]. Cloisite 20A nanoclay powders with a cation exchange capacity of 95 meq/100 g were generously provided by BYK® (BYK-Chemie GmbH, Germany). Cloisite microclays were produced when naturally occurring montmorillonite microclay minerals were modified with ammonium organic hydrogenated tallow modifiers, and Na^+ cations were replaced by the modifier. These products exhibit enhanced hydrophobicity with varying properties and functionalities. As a baseline, a conventional lithium soap-based grease with a 10.6% thickener concentration in PAO10 base oil was created according to a standard protocol [45]. Pure oleic acid, ethyl alcohol, and toluene were purchased from Sigma-Aldrich, USA.

2.2 Grease formulation and naming convention

The following steps were followed to prepare each grease sample. Nanoclays, previously dried at 60 °C for 1 h, were first added to 200 mL of toluene and mixed with a magnetic stirrer at 500 r/min for 30 min before sonicating for another 30 min in a 70 W, 40 kHz ultrasonic bath. Separately, with a volume ratio of 1:50, oleic acid was dissolved in pure ethanol and sonicated for 30 min. To functionalize the nanoparticles, an oleic acid-ethanol mixture was then added to the activated nanoparticle-toluene mixture, magnetically stirred at 300 r/min for 10 min, and placed in an ultrasonic bath for another half an hour. The base oils were finally added to the functionalized nanoclay mixture and mechanically stirred (Fisher Scientific, USA) for 24 h at 200 r/min using a 50 mm impeller, while being heated at 120 °C to evaporate both toluene and ethanol. To ensure that the temperature remained constant during stirring, the glass beaker containing the sample was placed in a crystallizing dish filled with oil, and its temperature was controlled using an external temperature probe. The weight ratios were selected such that the final mass ratio of nanoclay to oleic acid was 10:1.

Four groups of greases were first prepared by dispersing 5, 10, 15, and 20 wt% of functionalized nanoclays into PAO10 synthetic oil, and initial tribological tests were performed. Because the tribological response of the higher nanoclay concentration greases was not satisfactory, the next groups of greases were only made with 5 and 10 wt% loadings of nanoclays in the base oils. The results of the initial wear tests, including 15 and 20 wt% PAO10-based greases, are presented in Fig. S1 in the Electronic Supplementary Material (ESM). Further tests and characterizations were only conducted on the lower concentration samples, that is, 5 and 10 wt%. In naming the samples, first, a number showing the clay concentration is mentioned, followed by the base oil name or abbreviation; for instance, 5PAO represents a PAO10-based sample with a 5 wt% concentration of thickener.

2.3 Physicochemical characterization

2.3.1 Rheological measurements

The viscosity flow behavior of the samples was characterized using a highly accurate air-bearing motor rheometer (MCR 92, Anton Paar, Austria). A parallel plate setup was used for the base oils, whereas a cone and plate configuration was used for the greases. Before and after each assessment, the measuring device and stage were cleaned with toluene, hexane, acetone, and isopropanol. A lint-free tissue was used to clean them, and in the end, they were

completely dried with a manual air blower. The temperature of the samples was controlled using a thermoelectric module while they were enclosed in the chamber.

The temperature dependency of the viscosity of the base oils was evaluated using a parallel plate configuration with a 25 mm diameter measuring plate. The gap was set at 100 μm, and the rotational mode measurements were performed at a shear rate of 50 s^{-1} in the temperature range of 20–150 °C. The same configuration was utilized to determine how the viscosity of the base oils changed with the shear rate.

For the greases, to avoid test artifacts such as edge fracture and slip effects, a cone and plate geometry with 50 mm diameter and 1° cone angle was used according to DIN 91143-2 standard. The gap size at the center of the cone was 0.096 mm. The changes in viscosity as the temperature increased were measured in the temperature range of 20–150 °C. The viscosity of the grease was also measured as a function of the shear rate at room temperature.

2.3.2 Contact angle measurements

The hydrophobicity of grease is an important characteristic because it is related to its ability to protect components from corrosion and resist degradation by moisture in the working environment. For bio-based lubricants, which can sometimes be more susceptible to water absorption or hydrolysis than their synthetic counterparts, exhibiting a high degree of hydrophobicity is particularly important. To quantitatively measure the hydrophobicity of the formulated grease surfaces, contact angle measurements were conducted using the Sessile water drop method using a contact angle goniometer (DataPhysics OCA 15EC, DataPhysics, USA) equipped with a CCD video camera.

2.4 Tribological performance evaluation

2.4.1 Tribometer setup and test conditions

Purchased from McMaster Carr (Elmhurst, IL, USA), test tribopairs were AISI 52100 steel, with root-mean-square roughness of 10–30 nm and elastic modulus of 200–210 GPa. The hardness value for the 6-mm-diameter counterbodies was 800–900 HV, and that of the 1-inch mirror-polished flats was 720–780 HV. Before tests, both the substrates and counterbodies were sequentially cleaned by first rinsing in toluene and then sonication in n-hexane for 15 min, before another 15 min sonication in acetone. They were then dried using, first, a lint-free wipe and finally compressed nitrogen gas. The tribometer disk and counterbody holders were cleaned after each experiment by sonicating in acetone, then rinsing three times in isopropanol, followed by drying with compressed air.

To best replicate the realistic operational conditions, the macroscale tribological tests were carried out in the reciprocating mode using a tribometer (Phoenix TE-77, Phoenix Tribology Ltd., UK) with a stroke length of 10 mm. This arrangement is designed [46] to simulate oscillatory and repeated contacts in service, such as piston ring-cylinder liner segments, start-stop/vibrational point contacts (e.g., cam/follower screening), and grease-lubricated oscillating bearings such as wind-turbine pitch/yaw [47–49]. The motion followed a sinusoidal velocity profile, and all reported velocities are the calculated average linear velocity (v_{avg} = 2 × stroke length × frequency). Each test was repeated at least 3 times. In the first set of tribology experiments, the effect of velocity was assessed. Velocity sweep (VS) experiments were done under a 20 N load at laboratory ambient temperature (20–23 °C) and relative humidity RH = 35%. The starting average velocity was 0.2 mm·s^{-1}, and it continually rose to 500 mm·s^{-1}. The second set of tests used a continuous load ramp (LR) from 50 to 500 N under the constant average velocity of 400 mm·s^{-1}. To avoid plastic deformation false effects at the contact spot, the starting point of the test, that is, 50 N and 400 mm·s^{-1}, was reached by raising both parameters simultaneously while contact motion was already initiated under minimal load and starting velocity. In the third set of tribological tests, the same conditions as LR tests were followed while the temperature was set at 150 °C. All the tests started 5 min after the temperature was stabilized. To ensure consistent and fully flooded lubrication conditions for each experiment, a sufficient amount of grease (approximately 0.5 g) was applied to the disk using a new, disposable spatula. The grease was carefully smoothed to ensure complete coverage of the contact path before the start of each test, and it was discarded after each experiment. To make sure the heating cycle would not affect the test results, after exposure to 150 °C, substrates were not used again for any other test.

2.4.2 Post-tribology surface analysis

Following the tribological tests, the wear tracks on the disks and the corresponding counterbody surfaces were chemically analyzed using a Raman Spectrometer (Renishaw Confocal, Renishaw, USA). To examine the formation of any tribofilm, Raman maps of selected areas on the wear tracks were generated. These maps were acquired using a green laser (532 nm) operating at a low power setting of 10% to mitigate any potential laser-induced artifacts or any damage to the surface. Each pixel in the map represents a spectrum collected with an exposure time of 0.5 s and an accumulation of 3 scans. To acquire higher resolution and lower noise spectra for detailed chemical analysis, specific points inside and outside the wear track were selected from the maps and further analyzed with an increased acquisition time, accumulating 50 scans per point.

An optical interferometer (Filmetrics, KLA Instruments, USA) equipped with a green light source was used to analyze a section of the wear tracks for wear volume measurements, producing detailed 3D profiles and extracting profile graphs. The same assembly was used to achieve the 3D interferometry visualization from the wear scar on the counterbodies.

Wear was quantified after completion of each tribological test by measuring the final dimensions of the wear features. Following standard practice for pin-on-disk reciprocating tests, the wear parameters chosen were the average width of the wear track on the disk and the average diameter of the wear scar on the counterbody. It is well-established that in this geometry, the wear track width on the stationary disk and the wear scar on the moving pin are different due to different contact times and stress cycles. Some known reasons for this phenomenon include spatial confinement of wear on the counterbody [50], distribution of wear over the stroke length of the disk [51], difference in actual sliding length per contact area (different kinematics) [50], and formation, trapping, and recirculation of the wear debris [52]. These measurements were conducted using the calibrated imaging software of a digital optical microscope (KEYENCE VHX-7000, KEYENCE Corporation of America, USA). The microscope was equipped with different types of light sources; therefore, in analyzing the optical pictures, the most informative light source was utilized. For each sample, the reported value is the average of at least ten measurements taken at different locations along the wear track or across the wear scar to ensure a representative result. Wear track measurements were focused more on the middle section of the stroke, where the absolute linear velocity was the highest and, therefore, the wear was more considerable.

3 Results and discussion

3.1 Base oils properties

The incorporation of montmorillonite nanoclays as thickening agents in grease formulation depends on complex physicochemical interactions between the clay's functional groups and fatty acid components. These interactions determine the structural integrity, thermal stability, and tribological performance of the resulting lubricant. Studies indicate that montmorillonite's layered structure, surface acidity, and cation exchange capacity work synergistically with fatty acid chain length, saturation, and carboxyl reactivity to form internal networks that enhance energy dissipation and wear resistance [39, 40].

Table 1 summarizes the composition of the oils used in preparing the samples. PAO10 synthetic oil is created by synthesizing 1-decene, a hydrocarbon with a 10-carbon chain (C10). Decene is a straight-chain alkene with the chemical formula $C_{10}H_{20}$, which has a double bond between the first and second carbon atoms. During the PAO10 synthesis process, these straight-chain alkene 1-decene molecules link together, and the resulting molecules typically range from about 20 (dimer) to 30 (trimer) carbon atoms, depending on how many 1-decene units combine. The final mixture would contain 10%–20% dimer, 50%–70% trimer, and 10%–30% tetramer. The starting material, 1-decene (C_{10}), is almost entirely consumed during polymerization, so free C_{10} monomers are not present in the final product [16].

Determined using gas chromatography-mass spectrometry (GC-MS), Fig. 1(a) shows, in mol fractions, the main fatty acid constituents of the other three base oils used. The triglycerides that form castor oil are glycerol molecules esterified with three fatty acid chains. As can be seen in the chart, about 85% of these fatty acids are ricinoleic acid (C18:1–OH), an 18-carbon fatty acid ($C_{18}H_{34}O_3$) with a hydroxyl group (–OH) on the 12th carbon, and a cis double bond between carbons 9 and 10. The rest includes smaller amounts of oleic acid (C18:1, one double bond), linoleic acid (C18:2, two double bonds), and traces of saturated fatty acids like stearic (C18:0) and palmitic (C16:0). The hydroxyl group makes ricinoleic acid polar and reactive, contributing to castor oil's high viscosity, lubricity, and biodegradability but also its susceptibility to oxidation and thermal breakdown compared to PAO10 [53].

Table 1 Structural features of the base oils

Oil type	Primary carbon chains	Dominant component	Key structural features	Functional groups	Double bonds	Predominant conformation
PAO10	C20–C40	Decene oligomers connected together	Branched, saturated hydrocarbons	None (no oxygen)	—	Extended, random
Castor	C18	Ricinoleic acid (C18:1; –OH)	Unsaturated, with hydroxyl group	One OH group	1 (cis)	Semi-extended, hydrogen-bonded
Rapeseed	C22	Erucic acid (C22:1)	Monounsaturated fatty acids	Carboxyl group	1 (cis)	Interdigitated, partially aligned
OV	C16–C24, C24 diOH-FAs	TAG estolides	Mix of saturated/unsaturated, dihydroxy C24	Carboxyl, two OH groups	Multiple	Branched, fractal networks

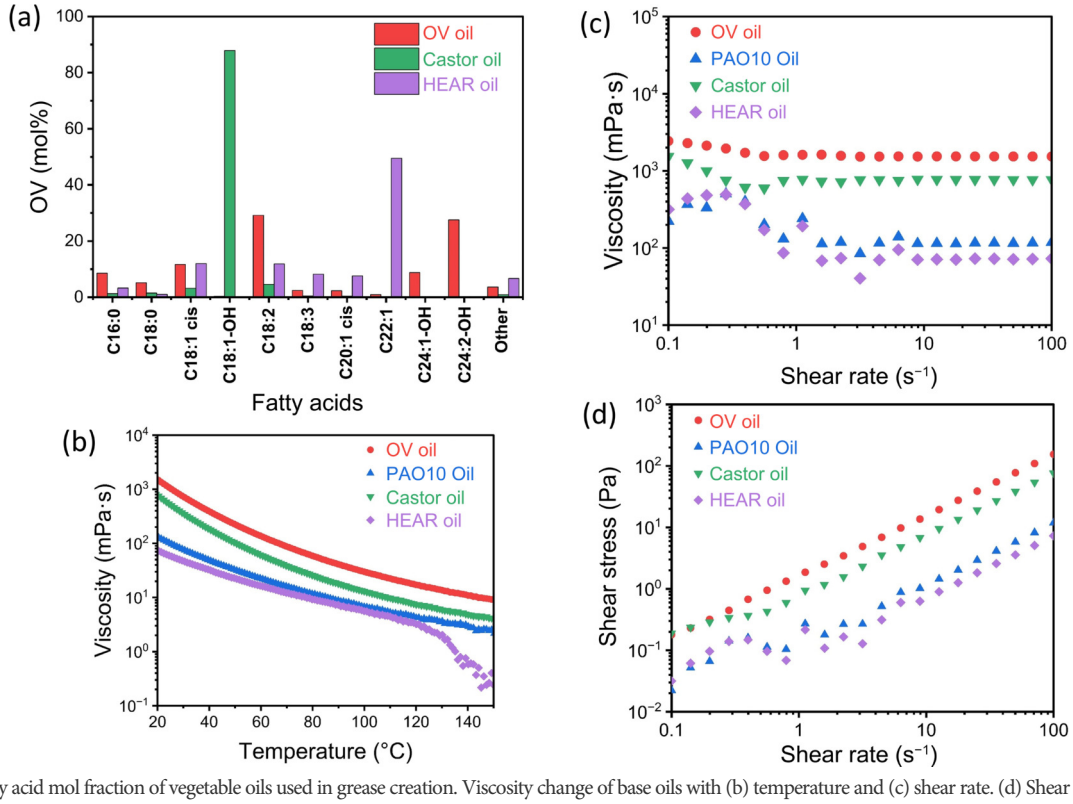

Fig. 1 (a) Fatty acid mol fraction of vegetable oils used in grease creation. Viscosity change of base oils with (b) temperature and (c) shear rate. (d) Shear stress change of base oils with shear rate.

HEAR oil, another triglyceride-based vegetable oil, as expected, is dominated (49.5%) by erucic acid, a 22-carbon monounsaturated fatty acid ($C_{22}H_{42}O_2$ or C22:1) with a cis double bond between carbons 13 and 14. The rest typically includes oleic acid (C18:1, 12.7%), linoleic acid (C18:2, 11.9%), linolenic acid (C18:3, 8.2%), and minor saturated fatty acids like stearic (C18:0) and palmitic (C16:0). These long, unsaturated chains give HEAR oil good lubricity and relatively high viscosity, but the double bonds make it less stable than PAO10 under heat or oxidative stress [54].

OV oil features a mix of standard fatty acids from C16 to C24, including palmitic, oleic, and linoleic acids. Its unique C24 dihydroxy fatty acids (nebraskanic and wuhanic acids, 38%), with hydroxyl groups at positions 7 and 18, enhance its potential as an industrial lubricant with better high-temperature resistance than the other two candidate oils [24]. Table 1 compares the most important structural features of the base oils.

The viscosity change of the oils as a function of temperature is presented in Fig. 1(b), where the general trend is that at all temperatures, OV is the most viscous, followed by castor, PAO10, and HEAR, respectively. It would be expected that the longer the primary chain length, the higher the viscosity because of a higher molecular weight and more entanglement, but the results here show a different outcome. The higher viscosity of OV and castor, despite their shorter chains than PAO10, is due to the presence of hydroxyl functional groups, enabling them to create strong hydrogen bonding. OV benefits from two –OH groups, hence showing higher viscosity than castor. Rapeseed, on the other hand, lacks strong polar interactions and solely relies on weaker van der Waals forces; therefore, it shows lower viscosity than PAO10 with its longer, branched chains.

At room temperature, OV and castor show much higher viscosity than PAO10, but as the temperature rises, the curves converge. As the PAO10 is composed of long saturated hydrocarbon chains and does not contain oxygen atoms or polar functional groups such as hydroxyl, carboxyl, or ester, it is a non-polar lubricant with high thermal stability and low volatility [16]. The presence of the hydroxyl group in both OV and castor oil, on the other hand, enhances lubricity and metal adhesion but also increases susceptibility to oxidation and thermal breakdown compared to PAO10. However, the dihydroxy fatty acids (diOH-FAs) in OV are part of TAG estolides and offer superior high-temperature resistance and lubrication properties compared to castor oil [29]. The long, unsaturated chains in HEAR oil provide good lubricity and viscosity, but the double bonds reduce stability under oxidation, making it less durable than PAO10 for high-temperature applications [54].

Flow curves (shear stress/shear rate) and viscosity curves (viscosity/shear rate) of the oil samples are compared in Figs. 1(c) and 1(d). While the graphs display a straight line (Newtonian behavior) in most of the shear rates tested, shear thinning can be seen solely in the initial section of the range. For OV and castor, the changes occur at shear rates of less than 1 s^{-1}, whereas the constant, nearly linear change is seen for PAO10 and rapeseed after 10 s^{-1} is passed. To understand the reasons for this behavior, molecular formation at rest and under shear should be analyzed.

At rest, long, filamentary molecules of uncrosslinked polymers contract to form balls entangled with each other [55], but carbon chains in the oils show a different formation. In the case of castor oil, the ricinoleic acid-rich system shows that these molecules adopt semi-extended, interdigitated conformations rather than contracted spheres. The hydroxyl groups form intermittent hydrogen bonds with neighboring molecules, creating a loosely networked structure [56]. HEAR systems, on the other hand, form partially aligned, interdigitated chains with transient clustering of erucic acid tails. The long hydrocarbon chains form random arrangements, while double-bond kinks create localized disordered regions [57]. The TAG estolides in OV, however, adopt branched, interdigitated conformations stabilized by hydrogen bonding between hydroxyl groups of diOH-FAs and steric hindrance from estolide side chains, which prevent tight packing. This can give rise to fractal-like networks where estolide branches project radially, maximizing surface contact with adjacent molecules [28, 29]. At rest, PAO10 molecules adopt extended, random conformations due to high rotational freedom around single bonds. The absence of double bonds or polar groups minimizes intermolecular forces, favoring entropy-driven stretching [58]. Studies report that the higher the chain length of PAOs, the more significant the initial decrease in viscosity would be [59].

After exposure to a shear strain at different rates, the structure at the rest state changes. As explained earlier, hydrogen bonding due to the presence of hydroxyl groups in OV (two) and castor (one) makes them more viscous than the other oils at all shear rates. Under shear, the hydrogen bonds break, the chains align, and disentanglement of the molecules occurs, leading to shear-thinning seen in the initial parts of the graphs. For HEAR, lack of strong hydrogen bonding causes lower viscosity, driven by van der Waals forces and ester polarity. Its C22 chains are longer than castor's C18 but shorter than PAO10's C20–C40 average, and the double bond adds flexibility, reducing viscosity. The branched, saturated C20–C40 hydrocarbon chains of PAO10 without any polar groups can only form weak van der Waals forces and no hydrogen bonding, hence its viscosity is lower than OV and castor. The branching reduces chain entanglement, making it less viscous. The initial decrease in viscosity for all samples might have occurred because the molecular chains became more aligned in the shear direction, and the intermolecular interactions reduced with increasing shear.

3.2 Grease formulation, stability, and hydrophobicity

A schematic of the steps used to create grease formulations is shown in Fig. 2(a). The successful formulation of a lubricating grease is defined by its ability to form a stable, semi-solid structure that effectively immobilizes the base oil and functions as a lubricant. Before running any tests or characterizations on the grease samples, they were left untouched for a few months and then visually inspected to ensure they were stable. Photographs of the samples taken approximately 15 months after creation are presented in Fig. 2(b), showing no oil separation from the functionalized organo-modified nanoclays, confirming their sustained structural stability. While these materials can also be described as oleogels, their classification as "lubricating greases" in this study is based on their demonstrated long-term stability and their subsequent, successful performance in reducing friction and wear in tribological testing. Previous studies on similar systems have used both terminologies to describe the material [8, 42, 60]. When high-temperature applications are to be considered, grease robustness at high temperatures and oxidation resistance also must be evaluated. While a prior study demonstrated very high stability of OV oil (up to 300 °C), which was confirmed with mass spectroscopy analysis, we performed oxidative onset temperature (OOT) on some grease samples and the base oils. Results confirmed the stability of OV oil and its derivative grease (Fig. S2(a) in the ESM).

The introduction of organic cations into naturally occurring

montmorillonite influences its interaction with other materials, especially water [61]. In comparison to other clays, Cloisite 20A is less hydrophilic than natural clays such as Cloisite Na+, but more hydrophilic than other organo-modified clays such as C10A and C30B [62]. Prior studies demonstrated the formation of C–O bonds on the clay surface after oleic acid functionalization [8]. Oleic acid functionalization further enhances the Cloisite 20A hydrophobicity, improving its dispersibility in non-polar solvents [63]. The carboxylic group of oleic acid reacts with the hydroxyl groups on the nanoparticle surface, leading to a shift from hydrophilic to lipophilic properties [64], which is important for grease creation. The modification process replaces some naturally occurring inorganic cations in the clay with organic cations. While the unmodified montmorillonite clay with the theoretical formula of the $M_y^+(Al_{2-y}Mg_y)(Si_4)O_{10}(OH)_2 \cdot nH_2O$ does contain hydroxyl groups [65], the modification process with the quaternary ammonium salt reduces the number of these hydroxyl groups and leaves some hydroxyl groups on the edges of the clay particles [66]. To evaluate the stability of the greases without OA additions, a 20 wt% PAO10-base comparison sample was created using non-functionalized nanoclay (Fig. S2(b) in the ESM), where again it shows no signs of oil separation, and it is structurally stable, yet visually the sample looks very brittle compared to the functionalized grease with the same nanoclay loading. Notably, all formulated grease samples show quite similar water wetting characteristics, with PAO10-based grease having the largest water contact angle (Fig. 2(c)). The wetting and absorption of water are important characteristics of greases impacting their lubrication performance under various operating conditions [67–69]. In the case of biodegradable oils as base oils, water absorption characteristics must be carefully managed to ensure adequate lubrication performance [70].

The consistency of the grease formulations, which is an industrial index for their application, was evaluated from the rotational rheological measurements. To estimate the national lubricating grease institute (NLGI) grade, the yield stress of each sample was determined from the steady-shear flow curves. Following the methodology of Couronne et al. [71], these yield stress values were correlated to the cone penetration data to assign an estimated NLGI grade. The results (Table 2) show a strong

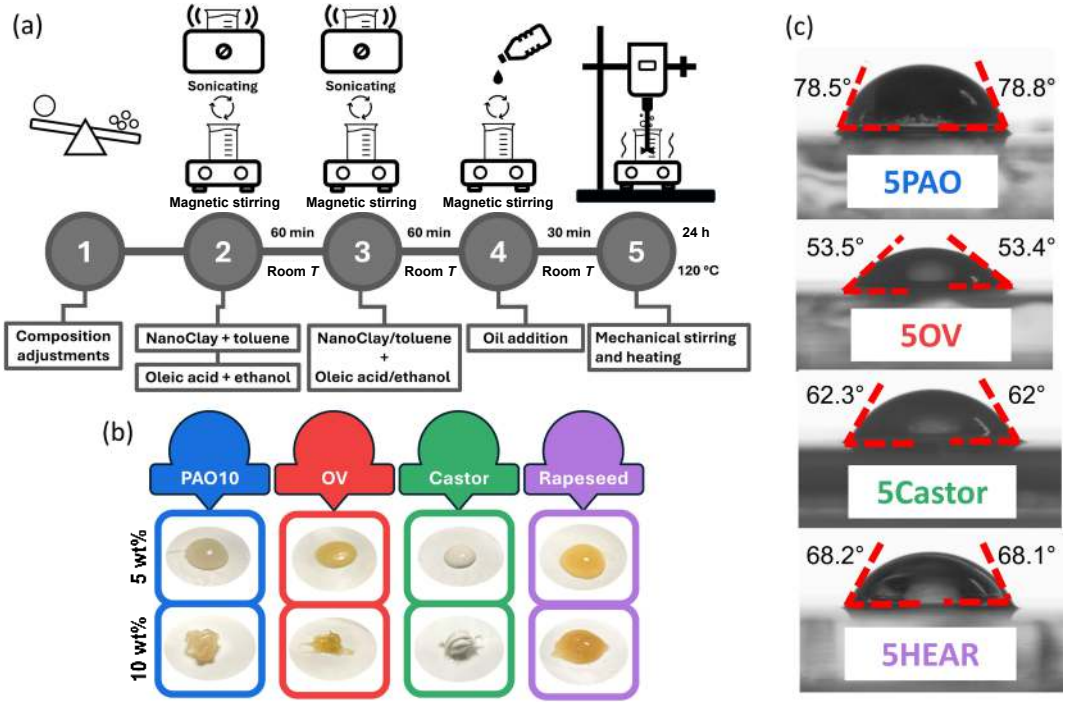

Fig. 2 (a) A schematic of grease creation steps. (b) Pictures of samples created. (c) Contact angle of a 2 μL water droplet on a surface coated with 5 wt% grease samples, demonstrating hydrophobicity of formulations.

Table 2 Estimated NLGI grade of formulated greases

Base oil	Concentration	Yield stress (Pa)[a]	Penetration (1/10 mm)[b,c]
PAO10	10 wt%	~800	280–300
	5 wt%	~8	~380–400
OV	10 wt%	~250	340–370
	5 wt%	~20	> 400
Castor	10 wt%	~80	~380–400
	5 wt%	~5	> 400
HEAR	10 wt%	~40	> 400
	5 wt%	~15	> 400
PAO10 (Li-soap thickener)	~10%	~330	340–360

Note: [a]Estimated from steady-shear flow curves at a shear rate of 0.1 s^{-1}. [b]Estimated by benchmarking yield stress against experimental data from Couronne et al. [71]. [c]Based on ASTM D217 penetration ranges.

dependence of grease consistency on both the thickener concentration and base oil type. The 10PAO grease was the firmest (NLGI 2), while the vegetable-oil-based greases were generally softer (NLGI 000-1), exhibiting soft consistency. As can be noted from these results, no acceptable grease-like performance will be achieved with loadings less than 5 wt%. This analysis highlights the utility of rotational rheometry for characterizing grease consistency. As noted by Couronne et al. [71], the yield stress determined from steady shear sweeps can be a more sensitive and mechanistically relevant parameter than both cone penetration and oscillatory amplitude sweep methods, as it directly measures the stress required to initiate flow. Interestingly, their work also showed that greases with a thickener concentration in the range of our samples closely followed the empirical "Plint's relationship" between the yield stress and cone penetration. This suggests that the flow curve can provide a reliable means of determining the physical properties of conventionally formulated greases.

3.3 Rheological behavior of formulations

3.3.1 Steady-shear behavior

The rheological performance of the nanoclay greases under steady shear rotational experiments is shown in Fig. 3. Figure 3(a) illustrates a several orders of magnitude increase in the viscosity of the samples compared to that of the base oils (Fig. 1(c)) at all shear rates. The higher the loading of the nanoclay thickener in the base oil, the higher the viscosity of the colloidal semi-solid grease. The graph also shows the shear-thinning non-Newtonian behavior of the greases, summarizing how the viscosity decreases with the shear rate. Again, this is contrary to the viscosity-shear rate behavior of the base oils, where, for the most part, their viscosity was independent of the shear rate. Looking at the 10 wt% samples, a striking result from these responses is the viscosity increase achieved after the addition of the nanoclays to the synthetic oil. Although PAO10 oil illustrates much lower viscosity than OV and castor oils, the greases made of it show much higher viscosity than those from polar bio-oils. The reason can be evaluated in terms of the molecular interactions between the carbon chains of the base oils and oleic acid-functionalized nanoclay particles.

In the case of PAO10, the interaction of the oil with the OA-functionalized Cloisite 20A is mostly physical, and the non-polar alkyl chains of both substances, the oil and the clay, align and mix well. However, because the PAO chains are saturated, there is no matching group for oleic acid, so there is limited chemical bonding; instead, dispersion forces play the key role. This improved compatibility helps nanoclay particles disperse better in PAO10 and enhances stability and viscosity. As for the polar vegetable base oils, the polarity of the base oil is an effective parameter that can influence the reactions with OA-functionalized Cloisite, affecting the viscosity responses we observe. When polar groups on a nanoparticle interact well with the solvent, they can improve dispersion and stability to a great extent, as seen with functionalized carbon nanotubes [72]. Polarity in molecules is influenced by the presence of polar functional groups, such as hydroxyl groups (the most effective), ester linkages, and double bonds, which influence charge distribution and interactions like hydrogen bonding [73]. Comparing OV, castor, and HEAR oils, mostly composed of branched TAGs, with PAO10 clarifies how difficult it is for them to intercalate into the layered nanoclays. As a result, the viscosity of the PAO10 grease is higher than that of vegetable-based oils, though the trend for the base oils is different. This can be attributed to differences in the network structure of the greases. The viscosity response of the nanoclay greases with temperature is plotted in Fig. 3(b). As expected, the general trend is reduced viscosity as temperature goes up because of the Brownian motion of the constituent molecules, leading to lower internal friction.

3.3.2 Oscillatory low-temperature performance

The performance and structural stability of lubricants at sub-zero temperatures are critical for ensuring reliability during operations in cold environments. To evaluate this, the rheological behavior of the 10 wt% nanoclay-based samples was compared with the lithium soap benchmark grease during a full freeze-thaw cycle from 25 to −20 °C and back to 25 °C (Fig. 4).

As expected, all grease samples exhibited an order of magnitude increase in the complex viscosity upon cooling, which was a consequence of the base oil thickening and reduced molecular mobility at lower temperatures. The degree of hysteresis, that is, the gap between the cooling and heating curves under oscillatory motion, provides information about the structural reversibility of the material after being subjected to thermal stress [55]. A small hysteresis loop, in which the heating and cooling curves follow each other closely, and the final viscosity at room temperature returns to its initial value, demonstrates a stable structure that is not permanently damaged by the cold thermal cycle.

All three formulations demonstrated excellent structural stability. The freeze-thaw curves for the 10OV, 10PAO, and lithium base greases (Fig. 4) show very narrow hysteresis loops, indicating that their thickener networks were resilient and recovered almost completely after experiencing cryogenic temperatures and a severe thermal shock. This suggests that under conditions of repeated cold starts, all three greases maintained

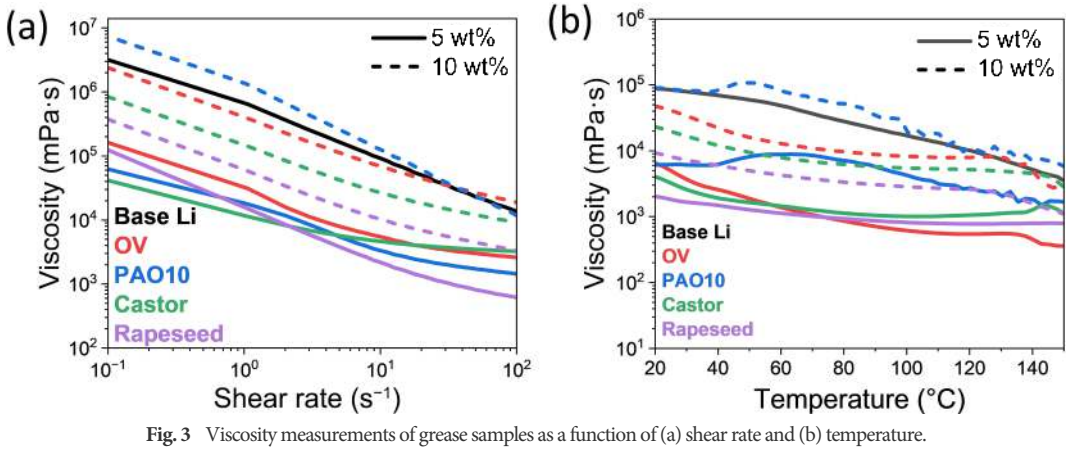

Fig. 3 Viscosity measurements of grease samples as a function of (a) shear rate and (b) temperature.

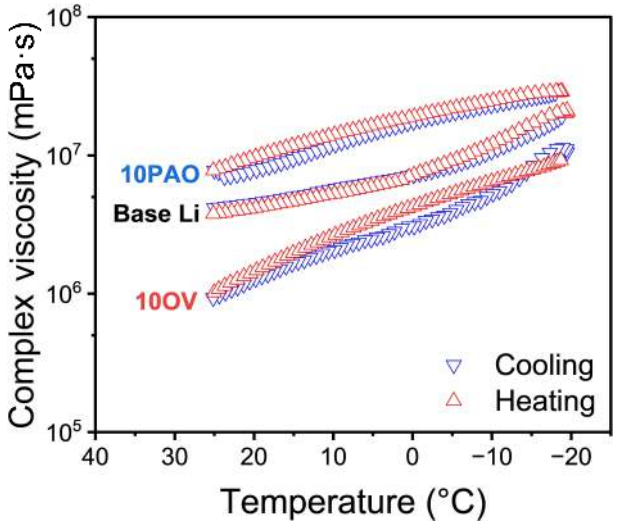

Fig. 4 Low-temperature rheological performance. Complex viscosity as a function of temperature in a freeze-thaw cycle (25 → −20 → 25 °C) demonstrates superior structural recovery of nanoclay-thickened samples, similar to an industrial benchmark.

their consistency and performance without experiencing significant degradation. Notably, the same order as the steady-state measurements was seen here, where 10PAO grease consistently preserved its highest complex viscosity across the entire temperature range, implying that it formed the stiffest structure, whereas 10OV grease was the least viscous of the three, a property that could be advantageous for reducing low-temperature drag and improving energy efficiency.

3.4 Tribological performance

3.4.1 VS

As stated earlier, because no acceptable results were achieved from nanoclay concentrations higher than 10 wt%, the grease samples were made only with 5 and 10 wt%. Figure S1(a) in the ESM demonstrates the VS response of the PAO10-based greases with 5, 10, 15, and 20 wt%. While 5 and 10 wt% samples show similar the highest coefficient of friction (COF) in the range of 0.06–0.08, the 15 wt% sample fluctuates considerably, suggesting instability in the friction performance, whereas 20 wt% exhibits the COF in the same range as an unlubricated steel on steel contact, implying a complete failure of the lubricant. Velocity does not seem to impact the lower-concentration samples but seriously affects the performance of the higher-concentration ones. To further make sure the two selected samples are the best performers when the velocity is the main variable, the same tests were also carried out under 100 and 200 N. Figures S1(b) and S1(c) in the ESM show that the results, even at these considerably higher loads, are satisfactory. It is worth mentioning here that the COF plots, are presented on a semi-logarithmic scale for visualizing purposes, and the values significantly change when transitioning from the low-friction hydrodynamic regime to the high-friction boundary regime, indicating signs of lubricant starvation at the contact.

Figure 5 compares the VS test results for all the grease samples. The graph in Fig. 5(a) indicates relatively similar friction behavior for all 5 wt% mixtures across the velocity range tested. There is a slight increase in the friction coefficient with velocity for some mixtures. For the 10 wt% samples (Fig. 5(b)), however, the differences in friction behavior are more pronounced. The baseline lithium grease did not perform well in this test and showed a higher COF with more fluctuations compared to the nanoclay-thickened greases. The 10OV sample appears to have a higher COF compared to the others, particularly at higher velocities. The 10PAO grease, on the other hand, failed to lubricate well at lower velocities, but as the velocity increased it showed a lower and more stable COF. The other two samples (castor and HEAR) show lower and more stable friction coefficients compared to the model lubricant and 10OV and 10PAO samples.

The friction performance of the oils is compared with that of the greases made based on them in Figs. S3(a)–S3(d) in the ESM. Figure S3(f) in the ESM compares the results for the base oils without any nanoclay additions. While all show acceptably low COF all along the test range, HEAR shows some instability at the highest velocities tested, like what is seen for the 10HEAR. It

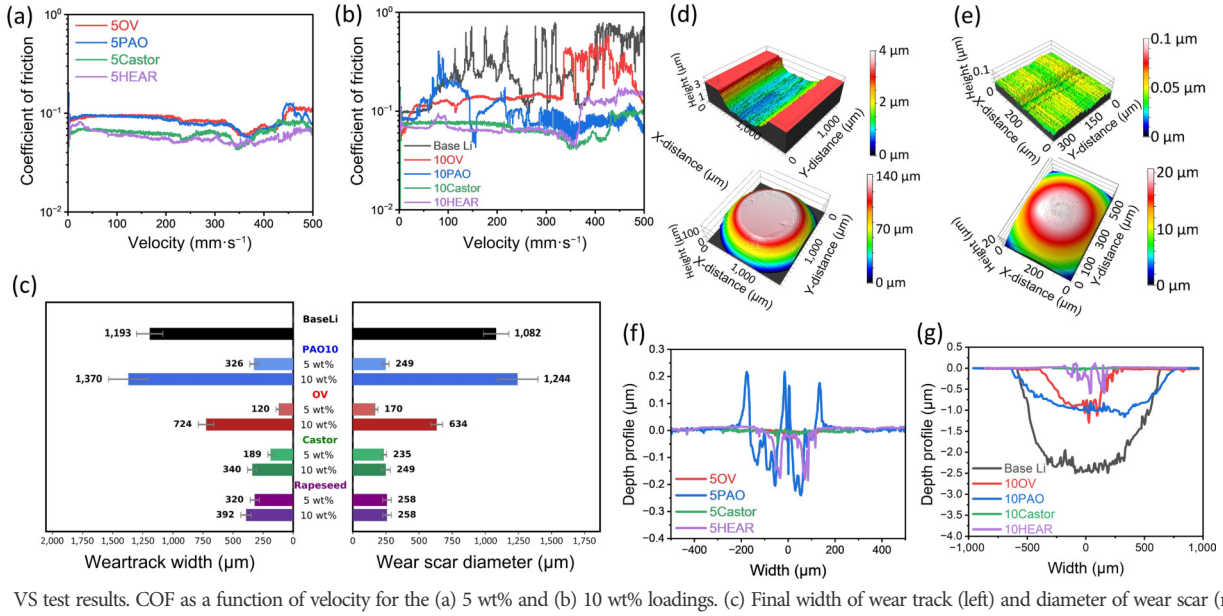

Fig. 5 VS test results. COF as a function of velocity for the (a) 5 wt% and (b) 10 wt% loadings. (c) Final width of wear track (left) and diameter of wear scar (right). Representative optical interferometry images of wear track and wear scar after testing with (d) lithium base grease and (e) 5OV grease. Representative 2D wear profiles of tracks for (f) 5 wt% and (g) 10 wt% greases.

suggests that 5 wt% could overcome the base oil's instability at velocities higher than 400 mm·s^{-1}, but higher loadings of the nanoparticles fail to replicate the same effect. That said, even in that region, the COF is acceptably low. Another noticeable point here is that the COFs achieved from 5 wt% greases are in the same range as the base oil, which is a great achievement. In conclusion, this figure shows that, apart from 10OV at high velocities and 10PAO at low velocities, both concentrations of the nanoclays could preserve the performance of the base oils, yet clearly without the need for submerging the contact into the lubricant.

To analyze the film-forming capabilities of the grease samples, the graphs of Figs. 5(a) and 5(b) can be assessed in the context of the Stribeck curve. The Stribeck curve is typically plotted for the COF changes against the Hersey number (viscosity × speed/load), and it helps to understand the different lubrication regimes: boundary, mixed, elastohydrodynamic, and hydrodynamic lubrication [74]. While these graphs are shown as a function of velocity, we can still see the lubrication regimes based on the trends.

Considering Fig. 5(a), all four 5 wt% samples exhibit a relatively similar behavior over the whole range of velocities with a relatively stable COF up to around 300–400 mm·s^{-1} (different in each case), where the COF starts to drop more. Because the initial stable COF can be regarded as low for this tribopair, the lubrication regime should be mixed, suggesting minor asperity contact, and as the COF starts to drop, lubrication falls into the elastohydrodynamic region, meaning fewer contacts and a more robust lubrication film. As the velocity further goes up, a shift towards hydrodynamic lubrication occurs, and the COF starts to rise. In the case of higher concentrated greases, as described earlier, only castor and rapeseed-based samples provided satisfactory lubrication over the whole range, and the other two, together with the model Li grease, failed to lubricate well at some points. The 10Castor and 10HEAR greases demonstrated a similar behavior to the 5 wt% greases, and the same assessment stands here.

The wear results of these tests are presented in Fig. 5(c), both for the substrate and counterbody. The original optical pictures from the samples can be found in Fig. S4 in the ESM, where the base oil results are also presented. These results are consistent with the COF response of the samples, as at a glance one can see that the highest wear amounts are those of the model Li grease as well as 10OV and 10PAO, where the former fail to show good lubrication at high velocities, while the latter had the same problem at the lower range. Amongst all, 5OV presents the lowest wear, which, when compared with submerging the contact in the base OV oil, yields even lower wear on the disk and comparable wear scar on the counterbody (Fig. S3(e) in the ESM).

A better understanding of the wear response of the samples can be achieved by looking at the wear profiles instead of solely the top-view wear width, presented in Figs. 5(f) and 5(g). While all 5 wt% samples represent a negligible amount of wear comparable to that of the base oils (Fig. S3(g) in the ESM), in the case of OV and, to some extent, castor, it is more pronounced, where hardly any wear can be distinguished, and the depth profile is in the same range as the disk's initial roughness. A 3D interferometry image of a section of the wear track for 5OV in Fig. 5(e) more clearly shows this and compares it with that of the lithium base grease presented in Fig. 5(d). It is also evident from the counterbody's interferometry picture, where only some very shallow scratches can be distinguished. As for the other two samples, 5PAO shows more plastic deformation, whereas for the 5HEAR shallow scratches are visible. By increasing the thickener concentration, the performance changes dramatically, and only castor and rapeseed show similar wear results. This is attributed to the higher viscosity of OV and PAO10 oils, which suppresses the flow and lubrication of the surfaces.

3.4.2 LR

The results for the second set of tribology tests, LR, are demonstrated in Figs. 6(a) and 6(b), comparing the COF as a function of load. Like the VS graphs, to better probe very low values of COF and better visualize the variations, it is presented on a logarithmic scale. Again, while the lithium base grease has performed acceptably in the load range experimented and stabilized after some initial fluctuations in the COF, both nanoclay loadings exhibit better performance. The first noticeable difference with the VS tests is the significant improvement in the performance of the OV-based greases, showing great load-bearing

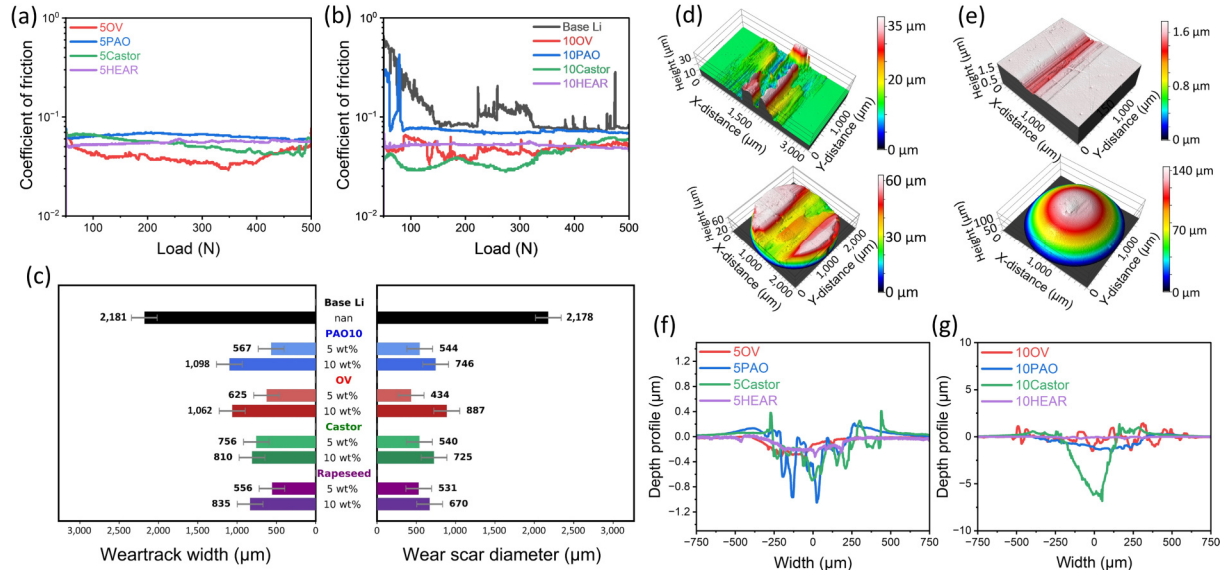

Fig. 6 LR tribology test results conducted at room temperature. COF as a function of load for (a) 5 wt% and (b) 10 wt% loadings. (c) Final width of wear track (left) and diameter of wear scar (right). Representative optical interferometry images of wear track and wear scar after testing with (d) Lithium base grease and (e) 5OV grease. Representative 2D wear profiles of tracks for (f) 5 wt% and (g) 10 wt% greases.

清華大学出版社 Tsinghua University Press | SciOpen

capacity of the base oil. This can be inferred from the COF response of the base oils (Fig. S5(f) in the ESM) with load. Under lower loads (< 250 N), all of the base oils show similar and acceptably low COF, yet as loads increase, all but OV start to show some instability. In the case of PAO10 and castor oil, it is more considerable, and a sharp spike, showing lubrication failure, is evident. Rapeseed, on the other hand, recovers very rapidly, which can be attributed to its lower viscosity. In the whole load range tested OV illustrated uniform COF regardless of the load.

The addition of the nanoparticles has greatly improved the stability of the lubricants, and all samples show consistent COF in the load range. As expected from the base oil tests, both OV concentrations exhibited great performance under load, contrary to what 10 wt% showed with velocity. The same is true for the PAO10-based greases; that is, while the 10 wt% sample did not perform well with velocity, it shows acceptable results with load. The addition of the nanoparticles to HEAR is interesting, where it preserved the same friction response of the base oil, regardless of the concentration (Fig. S5(d) in the ESM). As for castor, the 5 wt% sample exhibits a constant drop in the COF with load until the end of the range, where it slightly goes up. 10 wt% sample, however, is the best-performing sample under loads less than 300 N, and it gradually increases with load.

Looking at the wear results, almost all greases outperformed the base oils as well as the model Li grease by a great margin (Figs. S5(e) and S6 in the ESM). Interestingly, Fig. 6(c) demonstrates that the lower concentrations provided higher wear resistance. Depth profiles in Figs. 6(f) and 6(g) shed more light on the wear results of the samples. Whereas the wear depth is acceptably low for all 5 wt% greases, rapeseed, and OV base samples produced the lowest depth, castor, and PAO10 also show some deformation inside the wear track. Looking at the 10 wt% samples, rapeseed is the best performer, which can be attributed to its least fluctuating COF graph. OV's wear track is shallow with some plastic deformation, PAO10 produces a continuous wear track, and that of castor is narrower than the other samples but considerably deeper.

The interferometry picture of the wear track of the lithium base grease in Fig. 6(d) and that of the relevant counterbody in the lower part of that image show considerable amounts of material transfer from the counterbody to the substrate. The same has been witnessed for the PAO10 oil (Fig. S5(g) in the ESM), which presumably happened during the lubricant failure, seen from the spike in the COF curve. An optical shadow effect picture of the disk and counterbody after this test is shown in Figs. S7(a) and S7(b) in the ESM, where scuffing under high loads and inadequate lubrication is clear, and localized damage due to the formation of small welds between the surfaces can be seen. The interferometry picture of 5OV is also compared in Fig. 6(e), where the wear track is shallow, and the counterbody solely shows some superficial scratches.

To analyze the COF results of Figs. 6(a) and 6(b) in the context of Stribeck behavior, first, we need to keep in mind the fact that they are depicted as a function of load rather than speed, meaning lower loads often correspond to moving towards conditions that favor fluid film lubrication, the same condition as increasing speed. For the samples that show a straight line in the tested range (i.e., 5HEAR, 10HEAR, and 5PAO), an effective film has formed, which minimizes direct surface asperity contact, and the friction mechanism is dominated by shear within the lubricant film. In other words, the contact is probably operating in a full-film (elastohydrodynamic or hydrodynamic) lubrication regime. The other implication of these graphs is that over that range, the lubricants' shear behavior and film thickness do not vary significantly with contact load. This stability means that the lubricant is maintaining its load-carrying capacity, so the friction is controlled by the lubricant's inherent viscosity and rheology rather than by changing contact conditions.

Both loadings of castor and OV show a gradual change in the friction coefficient with the load. For all of them, the COF is already extremely low (lower than other samples), suggesting the presence of a stable lubricant film over the contact area. The change in the COF is indicative of moving from an elastohydrodynamic to a hydrodynamic regime. The load at which this change occurs for the 5 wt% samples is more towards the end of the range, around 350 N for OV and 480 N for castor, while for the more concentrated samples, it is in the first half of the test range, around 200 N for both. In the case of the other two samples, 10PAO and model lithium grease, at the beginning of the test, no stable film is present and, thus, the COF is considerable, but as the test continues full-film lubrication regime becomes prominent and controls the friction behavior. This transition for the PAO10-based grease occurs very rapidly but takes a while for the model grease to accommodate.

3.4.3 High-temperature LR

Figure 7 illustrates the high-temperature wear test results, the final group of tribology experiments. Once again, nearly all samples provided better lubrication than the lithium base example grease, with only 10PAO as an exception, showing a similar response and still not worse. Comparing Figs. 7(a) and 7(b) demonstrates that the overall COF trend for both concentrations is very similar in each group. Comparing two concentrations also highlights the smoother COF graphs for the 5 wt% samples and less noise in the results, approximately for all samples. PAO10-based samples show a gradual increase in the COF with load, but the overall rise is very negligible from around 0.066 to 0.155. Both greases created from rapeseed show a comparable performance to that of LR tests, that is a constant unchanged friction in the load range tested. The friction coefficient is, however, a little higher than the LR experiments, 0.06–0.07 compared to approximately 0.05, which can be attributed to the lower viscosity of the grease at higher temperatures. 5Castor and 10Castor samples exhibit a gradual decrease towards the middle range loads, and then COF goes up. It is more pronounced for the 10 wt% loading, though, which yields a higher starting COF, a steeper slope, and then an increase to higher coefficients than what 5 wt% gives.

The most striking results are achieved from OV-based greases. A deep U-shaped curve, characteristic of Stribeck curves, is evident where in the middle range, loads the COF drops to an even superlubricity regime (less than 0.01). It starts from approximately 200 N and continues up to around 340 N for the 5 wt% sample and 370 N for the 10 wt% sample. The least friction coefficient is achieved with 5 wt%, though. A very similar graph shape was observed in LR experiments for the 5OV sample, but here the COF is around an order of magnitude lower. It is worth mentioning that it is achieved without any additives, which shows the huge prospect of these greases in industrial real-life applications where different anti-friction, anti-wear, antioxidant, etc., additives are utilized to improve the performance of greases.

Different sections of each graph in terms of Stribeck behavior would be as follows. First, the low friction coefficient for all samples suggests that a uniform, well-lubricious film is formed, and direct asperity contacts are not considerable. The increase in the PAO10 greases might suggest either moving towards an elastohydrodynamic regime or remaining in the same

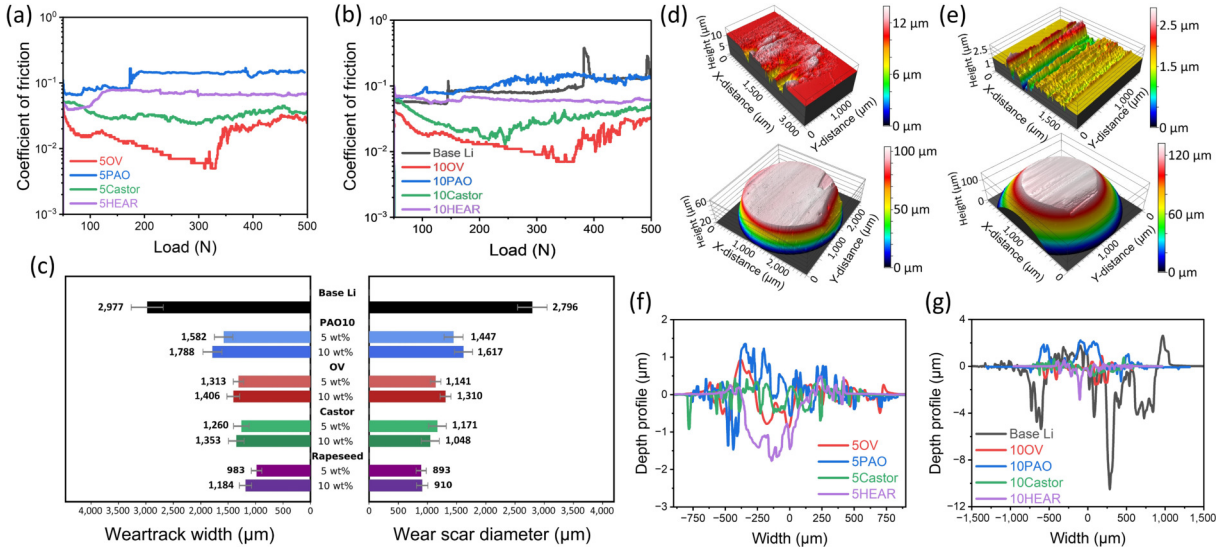

Fig. 7 High-temperature LR tribology test results conducted at a constant temperature of 150 °C. COF as a function of load for (a) 5 wt% and (b) 10 wt% loadings. (c) Final width of wear track (left) and diameter of wear scar (right). Representative optical interferometry images of wear track and wear scar after testing with (d) Lithium base grease and (e) 5OV grease. Representative 2D wear profiles of tracks for (f) 5 wt% and (g) 10 wt% greases.

elastohydrodynamic or hydrodynamic regime. The constant COF of the rapeseed samples, however, implies that no change in the lubrication regime is occurring. The U-shaped curve for castor and OV, on the other hand, can be because of a regime change. Keeping in mind that the graph is in terms of increasing loads, the slope towards lower COF, superlubricity in the case of OV, is a shift to elastohydrodynamic from the hydrodynamic regime. Further raising the contact pressure, which gives rise to higher frictions, is a sign of switching from an elastohydrodynamic to a mixed lubrication regime.

Figure 7(c) represents the wear results of the samples, and the optical images are shown in Fig. S9 in the ESM. It should be noted that the overall higher wear track width of the disks and wear scar diameter on the counterbodies can be attributed to the lower base material's strength and much higher oxidation rate at high temperatures. As the figure shows, contrary to LR results (Fig. 6(c)), where 5 wt% loadings were better lubricants than 10 wt% ones, here, two groups show very close results. However, it can be said that again the lower concentration is more satisfactory. The rapeseed category shows the narrowest wear width here, whereas OV and castor are comparable, and PAO10 is the least favorable. As performed for previous test sets, depth profiles are analyzed again to make a more reliable comparison. Sample 3D interferometry demonstrations of lithium base and 5OV greases from the tribopairs in Figs. 7(d) and 7(e), once again clarify the superiority of the OV-base grease. Depth profile graphs for the two concentrations are shown in Figs. 7(f) and 7(g). Comparing these graphs shows that the scratches and surface deformations are shallower when 5 wt% loadings are incorporated. Amongst all samples, both concentrations of OV and castor provided acceptable levels of surface protection, while the model Li grease was the worst performing. PAO10-based greases show more plastic deformation, whereas the rapeseed group results in some scratches.

Comparisons between the grease and the base oils from which they are created can be found in Fig. S8 in the ESM. The COF graphs show that thickener addition to the oils in most cases preserved the lubrication performance in the same range, and in the case of castor, has even enhanced it. As for OV, up to around 350 N loads, the greases performed better than the oil, but at the highest load range, the oil showed a continuous decrease in COF to the extremely low range. While the wear widths that are extracted using an optical microscope show lower values for the oils, depth profiles clarify that these narrower scratches are much deeper than greases and accompany considerable material removal, plastic deformation, and material transfer. One example optical image from testing with HEAR oil is shown in Figs. S7(c) and S7(d) in the ESM, which is very similar to the LR testing with PAO10 oil (Figs. S9(a) and S9(b) in the ESM), where severe wear because of inadequate lubrication occurred. Interestingly, while the HEAR oil could not perform a stable lubrication at high temperature, probably due to the loss of viscosity at temperatures higher than 130 °C (Fig. 1(b)), the addition of nanoclays preserved the lubrication and protected the surface during the experiment, as can be inferred from Figs. 7(f) and 7(g).

3.5 Mechanistic analysis of tribological behavior and tribofilm formation

The tribological results revealed a strong base oil responsiveness, with the dominant lubrication mechanism being a function of the specific chemistry of the base oil and its synergy with the nanoclay thickener. The different performance of the greases under various conditions can be attributed to different mechanistic behaviors. The first and most conventional mechanism is observed with the PAO10-based greases. As a non-polar synthetic oil, PAO10 lacks functional groups that would promote strong adsorption or interaction with the organoclay surface. Consequently, its lubrication mechanism is the classical tribochemical decomposition of the oil under thermal and mechanical stress. The result is reflected in the formation of a carbonaceous tribofilm, as confirmed by the Raman analysis.

In contrast, the vegetable oils, with their polar TAGs, facilitate more complex boundary lubrication. The HEAR-based greases, for instance, exhibited remarkably stable friction (COF ≈ 0.04–0.07) in almost all experiments. This consistent performance can be attributed to its high concentration of erucic acid (C22:1). The long hydrocarbon chain of this monounsaturated fatty acid is reported to form highly effective adsorbed boundary films on steel surfaces, providing excellent lubricity and wear protection [22]. Similarly, greases made with castor oil, mostly composed of ricinoleic acid (C18:1–OH), demonstrated stable COF and performed even better than HEAR-based counterparts in some

tests. Interestingly, castor oil showed a very good synergy with the nanoclay, and the resulting greases showed a good thermal stability.

The OV-based greases improve their performance under high temperatures (as evidenced by Fig. S8(f) in the ESM). The unique molecular structure of OV oil, rich in dihydroxy fatty acids and TAG estolides [43, 44], provides two specific attributes: (1) the polarity and functionality for a strong synergistic interaction with the nanoclay surface, and (2) the exceptional thermal and oxidative stability (Fig. S2(a) in the ESM) to withstand the harsh conditions. Such a unique combination of properties gives rise to the thermo-mechanical formation of a low-shear solid nanoclay film that leads to superlubricity.

As seen, the performance ranking of the greases demonstrated considerable dependence on the temperature and the load. At room temperature, particularly in the low-load VS experiments, the main tribological contributors seem to be grease mobility and contact replenishment. The samples with the highest room-temperature viscosity, and hence higher yield point and NLGI grade (10OV, 10PAO, and lithium base), exhibit poor performance, reflected in high COF and considerable wear. This is attributed to the contact starvation, with stiff greases being pushed outside the sliding contact as they are too rigid to flow back and replenish the wear track. Meanwhile, the less viscous castor and HEAR-based greases, as well as 5OV and 5PAO greases, provide better replenishment and maintain a more consistent lubricating film under these specific low-load conditions.

At high temperature (150 °C), this limitation no longer persists. The viscosity of all greases decreases significantly, and all samples can effectively replenish the contact zone. The combination of sufficient mobility, high temperature, and high contact pressure provides the necessary thermo-mechanical activation for unique lubrication mechanism of OV oil. To provide direct, molecular-level evidence for this proposed mechanism, particularly the superlubricity achieved with the OV-based greases, post-tribology surface analysis using Raman spectroscopy was performed on the wear tracks and their corresponding counterbodies.

Raman analysis results (Fig. 8) revealed two distinct and competing lubrication mechanisms originating from the base oil chemistry. Three samples were selected for the evaluations; the best-performing grease 10OV, the worst-performing one, 10PAO, and a critical 10OV sample from a test that was intentionally stopped during the superlubricity regime. In the case of the 10PAO grease, the lubrication mechanism was dominated by the tribochemical decomposition of the base oil. The Raman spectra obtained from within the wear track (Fig. 8(g)) exhibit prominent D-band (~1,350 cm^{-1}) and G-band (~1,580 cm^{-1}) peaks, which are clear signs of disordered and graphitic carbon [3]. These features were absent on the surface outside the wear track. The corresponding Raman maps (Figs. 8(d)–8(j)) confirmed the formation of a continuous carbonaceous tribofilm on both the disk and counterbody. This indicates that the primary role of the nanoclay network in the PAO10 system is to act as a reservoir, holding the oil in place so that it can decompose under high pressure and temperature to form a carbon-based boundary film.

A substantially different mechanism was observed for 10OV

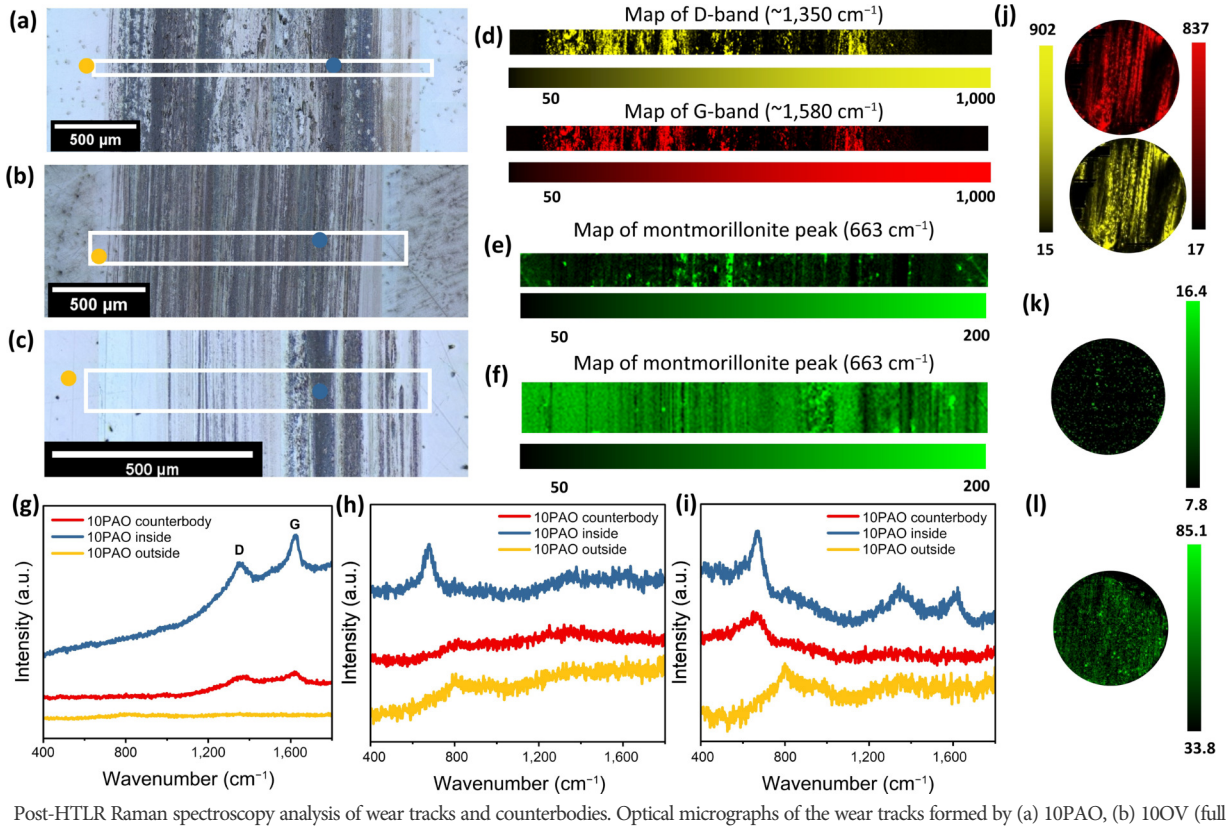

Fig. 8 Post-HTLR Raman spectroscopy analysis of wear tracks and counterbodies. Optical micrographs of the wear tracks formed by (a) 10PAO, (b) 10OV (full test), and (c) 10OV-S (test stopped during superlubricity). White boxes indicate mapped areas, with yellow and blue dots showing representative points outside and inside wear track, respectively. (d) Raman maps for the 10PAO wear track showing distribution of carbon D-band (~1,350 cm^{-1}) and G-band (~1,580 cm^{-1}). Raman maps for (e) 10OV and (f) 10OV-S wear tracks, showing distribution of characteristic montmorillonite peak (~663 cm^{-1}). Representative Raman spectra from outside wear track, inside wear track, and on the corresponding counterbody for (g) 10PAO, (h) 10OV, and (i) 10OV-S. Raman maps of counterbody surfaces for (j) 10PAO (D and G bands), (k) 10OV, and (l) 10OV-S (montmorillonite peak). Tests were performed at a constant temperature of 150 °C while increasing load. 10OV-S test was stopped at 350 N load.

grease. The Raman spectra from these wear tracks (Figs. 8(h) and 8(i)) show very weak carbon D and G bands barely visible inside the wear track. In comparison, the analysis revealed that the nanoclay thickener itself became the primary lubricating agent. A strong peak at approximately 663 cm^{-1}, characteristic of the montmorillonite clay structure, was found to be highly concentrated within the wear track (Figs. 8(e) and 8(f)). This demonstrates that under the contact area stresses, the nanoclay particles are not merely passive carriers but are actively drawn into the contact zone, where they are compacted to form a solid, protective tribofilm.

The unique chemistry of the OV oil appears to be the critical reason behind this mechanism. It is hypothesized that the polarity and specific molecular structure of fatty acids in OV oil create a superior synergy with the organo-modified clay surface. This interaction facilitates the exfoliation of the nanoclay particles under shear and promotes their adhesion to the steel surfaces. The result has been the formation of a continuous, low-shear solid lubricant film composed of aligned silicate platelets.

The comparison between the full-test (10OV) and the superlubricity-stopped (10OV-S) samples provides the definitive evidence. The intensity of the montmorillonite signal is significantly higher and more uniform in the 10OV-S sample (Fig. 8(f)), for which the test was halted at the point of minimum friction. This directly correlates the state of superlubricity with the presence of a well-formed dense nanoclay tribofilm. Interestingly, a weak signal corresponding to a carbonaceous boundary film is also more apparent in the 10OV-S spectrum (Fig. 8(i)) compared to the full-test sample (Fig. 8(h)). This can be inferred as a possible composite mechanism, where the initial formation of the superlubricity interface may involve a transient carbon layer that is later worn away or incorporated into the more dominant and durable nanoclay tribofilm. Regardless, the analysis confirms the formation of a robust clay-on-clay sliding interface between the disk and the counterbody (Fig. 8(l)). This is the main mechanism responsible for the extremely low friction coefficients observed.

4 Conclusions

This study reported on the formulation and comprehensive performance analysis of novel, sustainable greases made with vegetable oils and oleic acid-functionalized organo-modified nanoclay thickener. Through extensive characterization, the following most important conclusions were drawn:

(1) Successful design of high-performance bio-greases: Stable greases were successfully formulated using organo-modified nanoclay as a thickener with various vegetable and synthetic base oils. These greases consistently performed better than a standard industrial-grade lithium soap grease in reducing friction and protecting against wear.

(2) Standard cryogenic stability: Oscillatory rheology confirmed structural robustness of the bio-based greases during freeze-thaw cycles. The formulated greases exhibited a very narrow hysteresis during temperature changes, and the final complex viscosity after the thermal cycle returned to the initial value, meaning that no damage occurred to their structure.

(3) Novel lubrication mechanism leading to superlubricity: Post-tribology Raman spectroscopy revealed that the superlubricity observed in the OV-based grease is not due to the formation of a traditional carbon-based tribofilm. Instead, it is attributed to the *in-situ* formation of a compacted, low-shear solid lubricant film composed of the montmorillonite nanoclay itself. The unique chemistry of the OV oil helps create this novel, protective clay-on-clay sliding interface.

(4) Critical role of formulation synergy: The study highlights the critical synergy between the base oil chemistry and the nanoclay thickener. The concentration required to form a standard grease, its rheological behavior, and the lubrication mechanism were all shown to be highly dependent on the type of base oil used. This signifies the importance of considering all variables when designing next-generation sustainable lubricants.

Given their excellent thermal stability and the superior performance of the studied formulations, they are promising candidates for demanding applications such as in high-temperature industrial gearboxes, lubricating components in environmentally sensitive areas (for instance, agriculture or marine), or in centralized lubrication systems that require good grease mobility. While the results illustrate the great potential of the nanoclay-thickened, eco-friendly greases, future work should address their long-term performance and environmental adaptability. Key research areas include the mechanical shear stability and durability of these greases under long operating conditions, standardized oil bleed characteristics, as well as their performance in corrosive or high-humidity environments. Furthermore, rheological analysis would shed light on the reasons for the observed tribological responses of the designed greases. Finally, computational methods, such as molecular dynamics simulations, could provide invaluable molecular-level insight into the synergistic interactions between the base oils and the nanoclay particles, and help optimize and accelerate the design of the next generation of high-performance, sustainable lubricants.

Acknowledgements

The authors acknowledge the support of this work by the National Science Foundation (NSF) (Award No. 2323452). This work was performed in part at the University of North Texas' Materials Research Facility. Support from BioDiscovery Institute (BDI) at the University of North Texas is acknowledged. The support from the University of North Texas Tribology Center is also acknowledged.

Author contributions

Mohammad Eskandari: Writing—original draft, Validation, Investigation, Methodology, Conceptualization, Visualization. Ali Zayaan Macknojia: Methodology, Formal analysis. Asghar Shirani: Methodology, Investigation. Kent Chapman: Writing—review & editing, Supervision, Methodology, Investigation, Formal analysis. Diana Berman: Writing—review & editing, Writing—original draft, Resources, Project administration, Methodology, Investigation, Funding acquisition, Formal analysis, Conceptualization.

Availability of data and materials

The data that support the findings of this study are available from the corresponding author upon reasonable request.

Declaration of competing interest

The authors have no competing interests to declare that are relevant to the contents of this article.

Electronic Supplementary Material

Supplementary material is available in the online version of this article at https://doi.org/10.26599/FRICT.2025.9441204.

References

[1] Krim J. Friction and energy dissipation mechanisms in adsorbed molecules and molecularly thin films. *Adv Phys* **61**(3): 155–323 (2012)

[2] Holmberg K, Erdemir A. Influence of tribology on global energy consumption, costs and emissions. *Friction* **5**(3): 263–284 (2017)
[3] Al Sulaimi R, Eskandari M, Shirani A, Macknojia A Z, Miller W, Berman D. Effect of Cu and Ni inclusion on tribological performance of tribocatalytically active coatings in hydrocarbon environments. *Coatings* **14**(1): 61 (2024)
[4] Shirani A, Al Sulaimi R, Macknojia A Z, Eskandari M, Berman D. Tribocatalytically-active nickel/cobalt phosphorous films for universal protection in a hydrocarbon-rich environment. *Sci Rep–UK* **13**: 10914 (2023)
[5] Budinski K G, Budinski S T. *Tribomaterials: Properties and Selection for Friction, Wear, and Erosion Applications*. Materials Park (USA): ASM International, 2021.
[6] Jacques K, Joy T, Shirani A, Berman D. Effect of water incorporation on the lubrication characteristics of synthetic oils. *Tribol Lett* **67**(4): 105 (2019)
[7] Soodoo N, Bouzidi L, Narine S S. Fundamental structure–function relationships in vegetable oil-based lubricants: A critical review. *Lubricants* **11**(7): 284 (2023)
[8] Soltannia B, Martin-Alarcon L, Uhryn J, Govedarica A, Egberts P, Trifkovic M. Enhanced rheological and tribological properties of nanoenhanced greases by tuning interparticle contacts. *J Colloid Interf Sci* **645**: 560–569 (2023)
[9] Núñez N, Martín-Alfonso J E, Valencia C, Sánchez M C, Franco J M. Rheology of new green lubricating grease formulations containing cellulose pulp and its methylated derivative as thickener agents. *Ind Crop Prod* **37**(1): 500–507 (2012)
[10] Macknojia A Z, Eskandari M, Omotosho K, Martin M C L, Ayyagari A, Berman D. Superlubricity in solid lubricated sliding and rolling contacts. *Materialia* **37**: 102212 (2024)
[11] Holmberg K, Erdemir A. The impact of tribology on energy use and CO_2 emission globally and in combustion engine and electric cars. *Tribol Int* **135**: 389–396 (2019)
[12] Berman D. Plant-based oils for sustainable lubrication solutions: Review. *Lubricants* **12**(9): 300 (2024)
[13] Candela V G, Renata K, Oliver W, Dir J R C, Rosa R M, Carme H, Natalia F, Leitat E. Revision of the european ecolabel criteria for lubricants criteria proposal for revision of EU ecolabel criteria. Brussels: European Union, 2018: 87–95.
[14] Donahue C J. Lubricating grease: A chemical primer. *J Chem Educ* **83** (6): 862 (2006)
[15] Rawat S S, Harsha A P. Current and future trends in grease lubrication. In: *Automotive Tribology*. Katiyar J K, Bhattacharya S, Patel V K, Kumar V, Eds. Springer Singapore, 2019: 147–182.
[16] Rudnick L R. *Synthetics, Mineral Oils, and Bio-based Lubricants: Chemistry and Technology*. Boca Raton (USA): CRC Press, 2020.
[17] Canter N. Feature article: Grease additives: Important contributors not to be overlooked. *Tribol Lubr Technol* **68**: 28 (2012)
[18] Bart J C J, Gucciardi E, Cavallaro S. *Biolubricants: Science and Technology*. Amsterdam (the Netherlands): Elsevier, 2012.
[19] Saxena A, Kumar D, Tandon N. Development of lubricious environmentally friendly greases using synergistic natural resources: A potential alternative to mineral oil-based greases. *J Clean Prod* **380**: 135047 (2022)
[20] Anand O N, Chhibber V K. Vegetable oil derivatives: Environment-friendly lubricants and fuels. *J Synth Lubr* **23**(2): 91–107 (2006)
[21] Rac A, Vencl A. Performance investigation of chain saw lubricants based on new sunflower oil (NSO). *Tribol Schmier* **56**: 51–54 (2009)
[22] Al Sulaimi R, Macknojia A, Eskandari M, Shirani A, Gautam B, Park W, Whitehead P, Alonso A P, Sedbrook J C, Chapman K D, et al. Evaluating the effects of very long chain and hydroxy fatty acid content on tribological performance and thermal oxidation behavior of plant-based lubricants. *Tribol Int* **185**: 108576 (2023)
[23] Mortier R M, Fox M F, Orszulik S T. *Chemistry and Technology of Lubricants*. Dordrecht (the Netherlands): Springer, 2010.
[24] Li X J, Teitgen A M, Shirani A, Ling J, Busta L, Cahoon R E, Zhang W, Li Z Y, Chapman K D, Berman D, et al. Discontinuous fatty acid elongation yields hydroxylated seed oil with improved function. *Nat Plants* **4**(9): 711–720 (2018)
[25] Shirani A, Joy T, Lager I, Yilmaz J L, Wang H L, Jeppson S, Cahoon E B, Chapman K, Stymne S, Berman D. Lubrication characteristics of wax esters from oils produced by a genetically-enhanced oilseed crop. *Tribol Int* **146**: 106234 (2020)
[26] Lugt P M. A review on grease lubrication in rolling bearings. *Tribol T* **52**(4): 470–480 (2009)
[27] Rudnick L R. Synthetics, Mineral Oils, and Bio-Based Lubricants. Boca Raton (USA): CRC Press, 2020.
[28] Romsdahl T, Shirani A, Minto R E, Zhang C Y, Cahoon E B, Chapman K D, Berman D. Nature-guided synthesis of advanced bio-lubricants. *Sci Rep–UK* **9**: 11711 (2019)
[29] Chen X L, Zhang G J, Cui W J, Ge C B, Li B, Li M, Liu S C, Wang L. Recent advances in the nutritional value, chemical compositions, pharmacological activity, and application value of *Orychophragmus violaceus*: A comprehensive review. *Molecules* **29**(6): 1314 (2024)
[30] Cermak S C, Isbell T A. Synthesis and physical properties of estolide-based functional fluids. *Ind Crop Prod* **18**(2): 183–196 (2003)
[31] Zulkifli M F R. Tribological and thermal characterisation of palm grease with organic thickener. *J Oil Palm Res* **37**(3): 549–559 (2024)
[32] Săpunaru O V, Sterpu A E, Vodounon C A, Nasr J, Duşescu-Vasile C, Osman S, Koncsag C I. Lubricating greases from fried vegetable oil: Preparation and characterization. *Lubricants* **12**(6): 197 (2024)
[33] Anh N D, Van N H, Van Hien T. Study on synthesis of biodegradable polyurea grease using modified vegetable oil. *J Mil Sci Technol* (FEE): 279–284 (2022)
[34] Ravikiran, Kundargi S, Aravind S L, Akhil V M, Madhusudhana R. Rheological and tribological characterization of completely biogenic grease. In: *Recent Trends in Materials*. Springer Singapore, 2022: 155–162.
[35] Yang S S, Lai B B, Liu Z Z, Lou W J. The development of a fully renewable lubricant: The effect of ethyl cellulose on the properties of a polyhydroxyalkanoate (P34HB)-based grease. *Sustainability–Basel* **16**(10): 4149 (2024)
[36] Gorbacheva S N, Yadykova A Y, Ilyin S O. A novel method for producing cellulose nanoparticles and their possible application as thickeners for biodegradable low-temperature greases. *Cellulose* **28** (16): 10203–10219 (2021)
[37] Borrego M, Kuhn E, Martín-Alfonso J E, Franco J M. Assessment of the tribological performance of electrospun lignin nanofibrous web-thickened bio-based greases in a nanotribometer. *Nanomaterials–Basel* **13**(21): 2852 (2023)
[38] Bognár G, Vencl A. Experimental investigation of viscosity of glycerol based nanofluids containing carbon nanotubes. *Tribol Ind* **41**(2): 267–273 (2019)
[39] Maric T, Nasir M Z M, Mayorga-Martinez C C, Rosli N F, Budanović M, Szőkölová K, Webster R D, Sofer Z, Pumera M. Cloisite microrobots as self-propelling cleaners for fast and efficient removal of improvised organophosphate nerve agents. *ACS Appl Mater Inter* **11**(35): 31832–31843 (2019)
[40] Hao L, Fan K T, Zhang C C, Wang L, Xu H, Dong J X. Organic modification of synthetic montmorillonite by long- and short-chain quaternary ammonium salt to enhance the thickening ability. *Appl Clay Sci* **265**: 107671 (2025)
[41] Undabeytia T, Shuali U, Nir S, Rubin B. Applications of chemically modified clay minerals and clays to water purification and slow release formulations of herbicides. *Minerals–Basel* **11**(1): 9 (2021)
[42] Martín-Alfonso J E, Martín-Alfonso M J, Valencia C, Cuberes M T. Rheological and tribological approaches as a tool for the development of sustainable lubricating greases based on nano-montmorillonite and castor oil. *Friction* **9**(2): 415–428 (2021)
[43] Eskandari M, Macknojia A Z, Romsdahl T B, Cahoon E B, Chapman K D, Berman D. Structure and thermorheological properties of TAG-estolide lipid macromolecules from Orychophragmus violaceus seeds. *Int J Biol Macromol* **334**: 149166 (2025)
[44] Winfield D D, Evangelista R L, Moser B R, Hay W T, Winkler-Moser J K, Bantchev G B, Cermak S C. Physicochemical characterization of

Orychophragmus violaceus seeds and oil, a potential source of dihydroxy-fatty acids. *Ind Crops Prod* **234**, 121530 (2025)
[45] Bruce R W. *Handbook of Lubrication and Tribology. Vol. II: Theory and Design*, 2nd edn. Boca Raton (USA): CRC Press, 2012.
[46] ASTM G133-22. Standard test method for linearly reciprocating ball-on-flat sliding wear. West Conshohocken (USA): ASTM International, 2022.
[47] Pusterhofer M, Summer F, Wuketich D, Grün F. Development of a model test system for a piston ring/cylinder liner-contact with focus on near-to-application seizure behaviour. *Lubricants* **7**(12): 104 (2019)
[48] de la Presilla R, Wandel S, Stammler M, Grebe M, Poll G, Glavatskih S. Oscillating rolling element bearings: A review of tribotesting and analysis approaches. *Tribol Int* **188**: 108805 (2023)
[49] ASTM D6425-23. Standard test method for measuring friction and wear properties of extreme pressure (EP) lubricating oils using SRV test machine. West Conshohocken (USA): ASTM International, 2023.
[50] Kucharski S, Mróz Z. Identification of wear process parameters in reciprocating ball-on-disc tests. *Tribol Int* **44**(2): 154–164 (2011)
[51] Pawlus P, Reizer R. Profilometric measurements of wear scars: A review. *Wear* **534–535**: 205150 (2023)
[52] Godet M. The third-body approach: A mechanical view of wear. *Wear* **100**(1–3): 437–452 (1984)
[53] Mutlu H, Meier M A R. Castor oil as a renewable resource for the chemical industry. *Eur J Lipid Sci Tech* **112**(1): 10–30 (2010)
[54] Gunstone F. *Rapeseed and Canola Oil*. Boca Raton (USA): CRC Press, 2004.
[55] Mezger T G. *The Rheology Handbook*. Hannover (Germany): Vincentz Network, 2009.
[56] Yeboah A, Ying S, Lu J N, Xie Y, Amoanimaa-Dede H, Boateng K G A, Chen M, Yin X G. Castor oil (Ricinus communis): A review on the chemical composition and physicochemical properties. *Food Sci Tech–Brazil* **41**: 399–413 (2021)
[57] Wang P D, Xiong X J, Zhang X B, Wu G, Liu F. A review of erucic acid production in Brassicaceae oilseeds: Progress and prospects for the genetic engineering of high and low-erucic acid rapeseeds (*brassica napus*). *Front Plant Sci* **13**: 899076 (2022)
[58] Zolper T, Li Z, Chen C L, Jungk M, Marks T, Chung Y W, Wang Q. Lubrication properties of polyalphaolefin and polysiloxane lubricants: Molecular structure–tribology relationships. *Tribol Lett* **48**(3): 355–365 (2012)
[59] Chen Y J, He Z R, Wang H Q, Li Y M, Wang H. Rheological properties and lubricating film formation performance of very low-viscosity and biodegradable polyalphaolefins. *Lubricants* **13**(2): 62 (2025)
[60] Cao Z F, Xia Y Q, Xi X. Nano-montmorillonite-doped lubricating grease exhibiting excellent insulating and tribological properties. *Friction* **5**(2): 219–230 (2017)
[61] Panigrahi M K, Ganguly R I, Dash R R. Wetability and dielectric property of DL-PLA/CLOISITE 20A/PANI nanocomposite. *Int J Sci Res Arch* **11**(2): 391–406 (2024)
[62] Salehiyan R, Song H Y, Kim M, Choi W J, Hyun K. Morphological evaluation of PP/PS blends filled with different types of clays by nonlinear rheological analysis. *Macromolecules* **49**(8): 3148–3160 (2016)
[63] Yan H, Zhang X H, Wei L Q, Liu X G, Xu B S. Hydrophobic magnesium hydroxide nanoparticles via oleic acid and poly(methyl methacrylate)-grafting surface modification. *Powder Technol* **193**(2): 125–129 (2009)
[64] Huang J, Liang G Z, Lu G, Zhang J P. Conservation of acidic papers using a dispersion of oleic acid-modified MgO nanoparticles in a non-polar solvent. *J Cult Herit* **34**: 61–68 (2018)
[65] Mondal D, Mollick M M R, Bhowmick B, Maity D, Bain M K, Rana D, Mukhopadhyay A, Dana K, Chattopadhyay D. Effect of poly(vinyl pyrrolidone) on the morphology and physical properties of poly (vinyl alcohol)/sodium montmorillonite nanocomposite films. *Prog Nat Sci* **23**(6): 579–587 (2013)
[66] Mansoori Y, Akhtarparast A, Reza Zamanloo M, Imanzadeh G, Masooleh T M. Polymer-montmorillonite nanocomposites: Chemical grafting of polyvinyl acetate onto Cloisite 20A. *Polym Composite* **32**(8): 1225–1234 (2011)
[67] Cyriac F, Lugt P M, Bosman R. Impact of water on the rheology of lubricating greases. *Tribol T* **59**(4): 679–689 (2016)
[68] Thampi A D, Alokkan D, Biju G, Sasidharan B, Rani S. Influence of grease formulation parameters on the tribological property of rice bran oil based lubricating grease. *J Am Oil Chem Soc* **98**(7): 769–778 (2021)
[69] Gurt A, Khonsari M. An overview of grease water resistance. *Lubricants* **8**(9): 86 (2020)
[70] Nagendramma P, Kumar P. Eco-friendly multipurpose lubricating greases from vegetable residual oils. *Lubricants* **3**(4): 628–636 (2015)
[71] Couronne I, Blettner G, Vergne P. Rheological behavior of greases: Part I: Effects of composition and structure. *Tribol T* **43**(4): 619–626 (2000)
[72] Rajendran D, Ramalingame R, Adiraju A, Nouri H, Kanoun O. Role of solvent polarity on dispersion quality and stability of functionalized carbon nanotubes. *J Compos Sci* **6**(1): 26 (2022)
[73] Henkel S, Misuraca M C, Troselj P, Davidson J, Hunter C A. Polarisation effects on the solvation properties of alcohols. *Chem Sci* **9**(1): 88–99 (2018)
[74] Berman D, Rosenkranz A, Marian M. *Fundamental and Practical Aspects of Tribology*. Boca Raton (USA): CRC Press, 2024.

Mohammad Eskandari is a Ph.D. candidate at the Department of Materials Science and Engineering, University of North Texas, USA. His research focuses on tribological and rheological analysis of green lubricants, high-temperature tribology, bio-tribology, surface engineering, nanomaterials and metals.

Ali Zayaan Macknojia is a Ph.D. candidate at Materials Science and Engineering Department, University of North Texas, USA. His research areas include tribological performance of 2D materials, additive manufacturing of lubricious microstructures, high-temperature tribology, surface engineering, and nanomaterials.

Asghar Shirani received his Ph.D. degree in materials science and engineering from the University of North Texas, USA, in 2021. He joined Hydrotex company as a senior research scientist and, then, Qorvo Inc., USA, as a process development engineer. His research area covers tribology, rheology, 2D materials, electronic materials, and semi-conductors.

Kent Chapman is a Regents Professor at the Department of Biological Sciences at University of North Texas, USA. Chapman's research interests include biochemistry, plant cell biology, lipid signaling, and metabolic engineering. Among his many recent professional accomplishments, Dr. Chapman was awarded the Terry Galliard Medal in 2020 for his research contributions in plant lipid biochemistry, and in 2021 he was named a Fellow of the American Society of Plant Biologists (ASPB). He serves as

the executive editor for *Progress in Lipid Research* and reviewing editor for *The Plant Cell*. He also currently serves as the President of the American Society of the ASPB.

Diana Berman is an associate professor in the Department of Materials Science and Engineering, University of North Texas, USA. Her research focuses on understanding fundamental aspects of friction, wear, and lubrication of materials with a larger vision of how this knowledge can be applied in practice. She has published more than 100 papers in peer-reviewed journals, a book, and 4 book chapters. She also holds 10 patents (both US and international). Among her awards are TechConnect Innovation Awards (2016 and 2017), Ralph E Powe Junior Faculty Enhancement Award (2017), Society of Tribologists and Lubrication Engineers Early Career Award (2018), UNT Early Career Professorship Award (2020), NSF Early Career Award (2021), and Fulbright Scholarship (2023). She serves on editorial boards for *Tribology Letters* and *Nature Scientific Reports* and as a program chair for the Advanced Surface Engineering Division of the American Vacuum Society (AVS).